machines

MDPI

Article

Influence-Coefficient Method for Identifying Maximum-Load Configurations and Variable-Load Issues in Manipulators

Raffaele Di Gregorio * and Erkan Yilmaz

LaMaViP, Department of Engineering, University of Ferrara, 44122 Ferrara, Italy; erkan.yilmaz@edu.unife.it
* Correspondence: raffaele.digregorio@unife.it; Tel.: +39-0532-97-4828

Abstract: The dimensioning of general-purpose machines such as manipulators involves the solution of a number of preliminary issues. The determination of reference external loads and the identification of machine configurations that give the maximum internal load for each component are two of these issues. These two problems are commonly addressed through trial-and-error procedures based on dynamic modelling, which are implemented with the support of simulation software, since static analyses are commonly considered inadequate to solve them. Despite this, here, a technique based on influence coefficients and static analyses is presented which solves them. Such technique is also able to foresee and justify dynamic issues (i.e., possible vibrations, etc.) that could heavily affect the machine behavior. The effectiveness of the proposed technique is proved by implementing it on a 3T1R parallel manipulator. The presented design method is general and applicable to any type of non-overconstrained manipulator or mechanism.

Keywords: parallel manipulators; dimensional synthesis; kinetostatics; influence coefficients

Citation: Di Gregorio, R.; Yilmaz, E. Influence-Coefficient Method for Identifying Maximum-Load Configurations and Variable-Load Issues in Manipulators. *Machines* **2021**, *9*, 27. https://doi.org/10.3390/machines9020027

Received: 4 January 2021
Accepted: 26 January 2021
Published: 2 February 2021

1. Introduction

The mechanical design of manipulators has mandatory steps summarizable as follows: type synthesis [1–4], dimensional synthesis [1,2,4], and machine-element design [5–7]. Type synthesis identifies the machine topologies that meet the motion requirements, dimensional synthesis determines the values of the geometric parameters that affect the motion tasks the machine has to perform, and, finally, machine-element design chooses materials and sizes of each component of the machine.

The third step needs, as input data, the reference external loads applied to the machine and the identification of the machine configurations that give the maximum internal loads for each component. In general-purpose machines, such as manipulators, these input data are not straightforwardly obtainable from the design requirements and their deduction becomes even more difficult when dealing with parallel manipulators (PMs) since PMs' reachable workspace usually includes particular configurations, named "parallel" singularities [8–10], where the end effector cannot carry any (even infinitesimal) load without breaking down the PM.

Various performance indices were conceived for identifying PMs' reachable-workspace regions that are free and far from singularities, where safely locating the useful workspace [11–18]. These indices well identify kinetostatic issues and can be useful to perform the dimensional synthesis and to locate the useful workspace (see, for instance, [19,20]) far from singularities. Nevertheless, they fail in relating the "distance" from singularities to the actual internal loads of the links.

Other indices take into account also robot stiffness and dynamic performances [16–18,21–26]. These other indices require the knowledge of data (e.g., masses, stiffness, etc.) that are available at the end of the machine design. Therefore, they are certainly suitable for comparing already-built manipulators, but their use during design is not straightforward since it requires trial-and-error procedures.

In general, all these indices can help the design procedure, but do not provide sufficient pieces of information for determining the input data of PMs' machine-element design. This determination is commonly addressed through trial-and-error procedures based on dynamic modelling, supported by multi-body simulation software, due to the preeminent dynamic nature of the loads applied to a manipulator. This widely adopted procedure is not able to justify unforeseen/unwanted machine behaviors that come out from the simulations thus making difficult to intervene for eliminating them.

Here, an algorithm, based on influence coefficients and static analyses, is presented which provides sufficient pieces of information for determining the input data of PMs' machine-element design. The proposed algorithm is also able to foresee and justify dynamic issues (i.e., possible vibrations, etc.) that could heavily affect the machine behavior. Its effectiveness is proved by implementing it on a 3T1R parallel manipulator. The presented design method is general and applicable to any type of non-overconstrained manipulator or mechanism.

The proposed algorithm is a novel way of computing and using influence coefficients in the design of general-purpose machines, mainly ideated for PMs, which aims at integrating the design methodologies based on performance indices and/or extended multibody simulations by solving their lacks. Indeed, it can overcome the fact that performance indices are not able to provide sufficient data for the machine-element design, and that extended multibody simulations often do not provide sufficient pieces of information for intervening when an unforeseen phenomenon comes out from the simulations.

The paper is organized as follows. Section 2 provides some background and presents the novel technique. Then, Section 3 applies the proposed method to a 3T1R parallel manipulator. Eventually, Section 4 discusses the results and Section 5 draws the conclusions.

2. Materials and Methods

Most manipulators are based on non-overconstrained architectures [27]. Non-overcon strained manipulators become isostatic structures when the actuated joints are locked. The static analysis of an isostatic structure is sufficient to relate external loads to links' internal loads and involves the solution of a problem that is linear and homogeneous in the input (i.e., external loads) and the output (i.e., links' internal loads) variables [28]. This solution does not need to know the materials the links are made of and links' cross-sections, which is an ideal condition for tools to employ during design when materials and actual sizes of the links are not known since their choice/determination is the design goal. In addition, such static analyses are based only on equilibrium equations and can take into account an esteem of the dynamic loads among the known external loads thus simulating an inverse dynamic problem [27].

Problems that involve the solution of a linear system, as the above-mentioned static analyses do, can be addressed by using the superposition principle [29]. In the case of a static analysis, the linear system to solve can be put into the following canonic form

$$\mathbf{A}\,\mathbf{x} = \mathbf{y} \tag{1}$$

where $\mathbf{x} = (x_1, \ldots, x_r)^T$ is an r-tuple collecting all the scalar components, x_i for i = 1, ... ,r, of the known external loads applied to the isostatic structure, $\mathbf{y} = (y_1, \ldots, y_s)^T$ is an s-tuple collecting all the scalar components, y_j for j = 1, ... ,s, of links' internal loads, and $\mathbf{A}$ is an s × r rectangular matrix of coefficients whose entries depend on the manipulator configuration.

The linearity of system (1) allows demonstrating that (superposition principle) if $\mathbf{x}$ is writable as follows

$$\mathbf{x} = \sum_{p=1,n} \lambda_p \mathbf{u}_p \tag{2}$$

where λ_p, for p = 1, . . . ,n, are n scalar coefficients and $\mathbf{u}_p = (\delta_{1p}, \ldots, \delta_{rp})^T$ (where δ_{ip} is the Kronecker delta defined as follows: $\delta_{ip} = 0$ for $i \neq p$ and $\delta_{ip} = 1$ for i = p), for p = 1, . . . ,n, are n unit r-tuple, then

$$\mathbf{y} = \sum_{p=1,n} \lambda_p \mathbf{v}_p \tag{3}$$

with $\mathbf{v}_p = \mathbf{A}\mathbf{u}_p$ for p = 1, . . . ,n. Hereafter, $\mathbf{v}_p$ will be named *p-th influence-coefficient vector*.

During the design of a manipulator, once the dimensional synthesis has been completed, Equation (3) can be exploited for the determination of the maximum internal loads of the links by implementing the following steps:

(i). according to the type of motion [30] the end effector can perform, up to three independent unit forces and up to three independent unit moments are identified for characterizing the dynamic loads applied to the end effector during motion and the other dynamic loads reduced to the end effector;
(ii). the unit forces/moments determined in the previous step are transformed into $\mathbf{u}_p$ r-tuples to introduce into Equation (2) for computing the input data of Equation (1);
(iii). for each $\mathbf{u}_p$ determined in the previous step, the corresponding influence-coefficient vector $\mathbf{v}_p$ is computed for a discretized set of end-effector poses inside the useful workspace of the manipulator;
(iv). the so-determined $\mathbf{v}_p$ are analyzed for finding the maximum internal loads of each link due to each unit load $\mathbf{u}_p$ together with the corresponding manipulator configurations;
(v). by exploiting Equation (3), the maximum internal loads of each link determined in the previous step are combined to obtain the reference internal loads of each link to use for sizing the link in terms of material choice and cross-section.

This procedure, over providing the input data for the machine-element design, is able to highlight critical conditions due to unbalanced variable loads acting on the links, since it is a static calculus referred to dynamic loads, thus providing pieces of information that orientate the next steps of the manipulator design.

Next section exemplifies the procedure by applying it to the partially decoupled 3T1R PM shown in Figure 1.

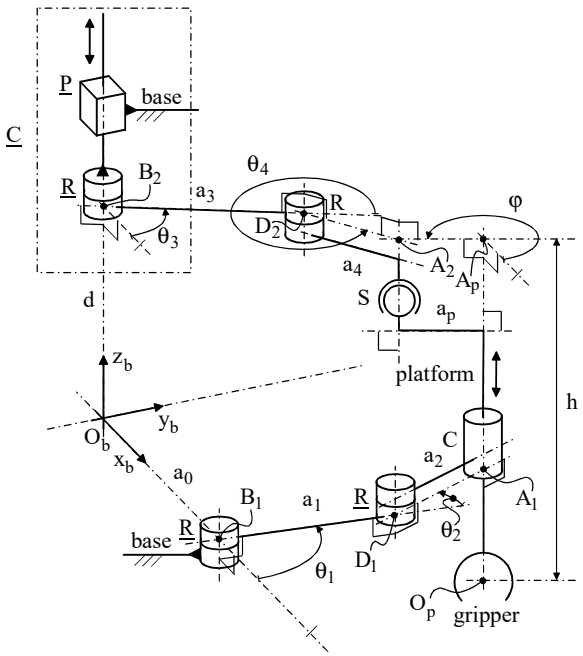

Figure 1. The 3T1R parallel manipulator of type C̲RS-R̲R̲C.

3. Results

Figure 1 shows a single-loop PM in which the end effector (platform) is simultaneously connected to the frame (base) through two kinematic chains (limbs), one of type $\underline{C}RS$[1] and the other of type $\underline{RR}C$, that is, it is a PM of type $\underline{C}RS$-$\underline{RR}C$. The axes of the R and C pairs are all parallel. The actuated C pair of the $\underline{C}RS$ limb is obtained by means of a PR chain with the sliding direction of the P pair parallel to the axis of the R pair. Such a PM architecture has four degrees of freedom [31] and constrains the platform to perform spatial translations (3T) plus rotations around axes with one fixed direction (1R), that is, the platform can perform only motions of 3T1R type, named Scara or Schoenflies motions [30]. This Scara PM has been ideated [20,31] at the Laboratory of Mechatronics and Virtual Prototyping (LaMaViP) of the University of Ferrara and, hereafter, for the sake of brevity, it will be named "LaMaViP's $\underline{C}RS$-$\underline{RR}C$". In the context of the Scara PMs, LaMaViP's $\underline{C}RS$-$\underline{RR}C$ is interesting because it can be actuated by keeping all the motors on the base and using commercial components, and it has the platform translation decoupled from the platform rotation [20,31].

The following notations/definitions are introduced (see Figure 1):

- $O_b x_b y_b z_b$ is a Cartesian reference fixed to the base with the direction of the z_b-coordinate axis parallel to the R and C pair axes;
- O_p is a point fixed to the platform whose coordinates, $(x_p, y_p, z_p)^T$, measured in $O_b x_b y_b z_b$, locate the position of the platform;
- B_2 is a point that lies on the axis of the actuated C-pair of the $\underline{C}RS$ limb and is fixed to the output link of the C-pair;
- d is the signed distance of B_2 from O_b chosen as linear joint-variable of the actuated C-pair;
- D_2, A_p, and A_2 are the intersection points between the plane parallel to the $x_b y_b$ plane that passes through B_2 and, respectively, the axis of the passive R-pair, the axis of the passive C-pair, and the line parallel to the z_b axis that passes through the center of the S-pair;
- h is a geometric constant of the platform equal to the length of the segment $A_p O_p$;
- a_p is a geometric constant of the platform that is equal to the length of the segment $A_p A_2$;
- φ is the angle between the segment $A_p A_2$ and the line parallel to x_b and passing through A_p (the angle φ uniquely determines the platform orientation);
- a_3 and a_4 are the lengths of the segments $B_2 D_2$ and $D_2 A_2$, respectively;
- θ_3 and θ_4 are the angular joint-variables of the actuated C-pair and of the passive R-pair, respectively;
- θ_1 and θ_2 are the angular joint-variables of the two actuated R-pairs of the $\underline{RR}C$ limb;
- B_1, D_1, and A_1 are the intersection points between the $x_b y_b$ coordinate plane and, respectively, the axis of the actuated R-pair adjacent to the base, the axis of the intermediate R-pair of the $\underline{RR}C$ limb and the axis of the passive C-pair;
- a_0, a_1 and a_2 are the lengths of the segments $O_b B_1$, $B_1 D_1$ and $D_1 A_1$, respectively.

From a kinematics point of view, the $\underline{RR}C$ limb constrains the platform to perform Schoenflies motions with rotation axis parallel to the z_b-coordinate axis and controls only the x_p and y_p coordinates of O_p (i.e., the platform translations parallel to the $x_b y_b$ coordinate-plane). Moreover, the $\underline{C}RS$ limb controls the coordinate z_p of point O_p (i.e., the platform translation parallel to the z_b-coordinate axis) through its linear joint-variable, d, and, independently, the platform orientation (i.e., the angle φ) through its angular joint-variable, θ_3.

[1] Hereafter, R, P, U, S, and C stand for revolute pair, prismatic pair, universal joint, spherical pair, and cylindrical pair respectively. With reference to a PM, which features the frame (base) and the end effector (platform) connected to each other by a number of kinematic chains (limbs), a string of capital letters denotes the sequence of joint types that are encountered by moving from the base to the platform on a limb. The hyphen separates the strings of the limbs and the underlining indicates the actuated joints. A serial architecture has only one limb and is denoted by only one string.

The dimensional synthesis of LaMaViP's CRS-RRC was addressed in [19]. In [19], a useful workspace assigned as a right circular cylinder with a radius, r_{uw}, of 300 mm and a height of 200 mm, whose axis is coincident with the z_b-coordinate axis, brought to choose the following values of the geometric constants (see Figure 1): a_0 = 800 mm, a_1 = 950 mm, a_2 = 600 mm, a_3 = 400 mm, a_4 = 400 mm, and a_p = 400 mm. Figure 2 shows the scaled top view of a LaMaViP's CRS-RRC sized according to this geometric data together with the position of the chosen useful workspace (the green circle in Figure 2). The analysis of Figure 2 reveals that the translation of the platform along the direction of the z_b-coordinate axis is fully decoupled from the remaining platform motion. Indeed, the motion due to the prismatic pair does not appear in the top view (Figure 2) where the PM becomes a planar six-bar mechanism controlled by the actuated-joint variables θ_1, θ_2, and θ_3. In addition, in this six-bar, θ_1 and θ_2 just control the position of the platform (i.e., the position of point A_1), whereas θ_3 fully controls the platform orientation (i.e., the angle φ) through a four-bar transmission.

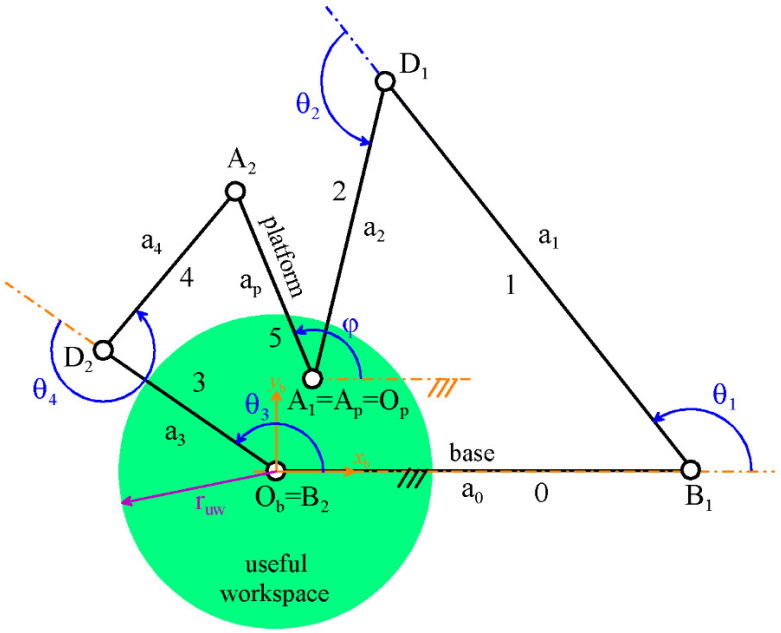

Figure 2. Scaled top view of a LaMaViP's CRS-RRC sized according to the results of the dimensional synthesis [19].

3.1. Implementation of Steps (i) and (ii)

According to the introduced notations, the 4-tuples $\mathbf{q} = (\theta_1,\theta_2,\theta_3,d)^T$ and $\boldsymbol{\kappa} = (x_p,y_p,z_p,\varphi)^T$ collect the actuated-joint (input) variables and the platform-pose (output) variables, respectively. The inspection of Figures 1 and 2 reveals that the entries of $\mathbf{q}$ and $\boldsymbol{\kappa}$ must satisfy the following constraint equations

$$x_p = a_0 + a_1\cos\theta_1 + a_2\cos(\theta_1 + \theta_2), \tag{4a}$$

$$y_p = a_1\sin\theta_1 + a_2\sin(\theta_1 + \theta_2), \tag{4b}$$

$$z_p = d - h \tag{4c}$$

$$(x_p + a_p\cos\varphi - a_3\cos\theta_3)^2 + (y_p + a_p\sin\varphi - a_3\sin\theta_3)^2 = {a_4}^2, \tag{4d}$$

which are holonomic and time-independent.

Equations (4a)–(4d) yield the following relationships between the virtual displacements $\delta\mathbf{q} = (\delta\theta_1, \delta\theta_2, \delta\theta_3, \delta d)^T$ and $\delta\boldsymbol{\kappa} = (\delta x_p, \delta y_p, \delta z_p, \delta\varphi)^T$

$$\mathbf{J}_k\delta\boldsymbol{\kappa} = \mathbf{J}_q\delta\mathbf{q} \tag{5}$$

with

$$\mathbf{J}_k = \begin{bmatrix} 1 & 0 & 0 & 0 \\ 0 & 1 & 0 & 0 \\ 0 & 0 & 1 & 0 \\ m_x & m_y & 0 & a_p(m_y c_\varphi - m_x s_\varphi) \end{bmatrix} \tag{6a}$$

$$\mathbf{J}_q = \begin{bmatrix} -(a_1 s_{\theta_1} + a_2 s_{(\theta_1+\theta_2)}) & -a_2 s_{(\theta_1+\theta_2)} & 0 & 0 \\ (a_1 c_{\theta_1} + a_2 c_{(\theta_1+\theta_2)}) & a_2 c_{(\theta_1+\theta_2)} & 0 & 0 \\ 0 & 0 & 0 & 1 \\ 0 & 0 & a_3(m_y c_{\theta_3} - m_x s_{\theta_3}) & 0 \end{bmatrix} \tag{6b}$$

where c_w and s_w stand for cos(w) and sin(w), respectively, whereas, (see Figure 2)

$$m_x = x_p + a_p c_\varphi - a_3 c_{\theta_3} = a_4 c_{(\theta_3+\theta_4)}; \quad m_y = y_p + a_p s_\varphi - a_3 s_{\theta_3} = a_4 s_{(\theta_3+\theta_4)} \tag{7}$$

The active-force[2] system applied to LaMaViP's CRS-RRC consists of the active external forces applied to the end effector and the generalized torques applied inside the actuated joints. The active external forces are collected into the 4-tuple $\boldsymbol{\gamma} = -(F_{e,x}, F_{e,y}, F_{e,z}, M_{e,z})^T$, where $F_{e,x}$, $F_{e,y}$, and $F_{e,z}$ are the components, along x_b, y_b, and z_b, respectively, of their resultant force and $M_{e,z}$ is the component along z_b of their resultant moment about O_p. In addition, the generalized torques are collected into the 4-tuple $\boldsymbol{\tau} = (\tau_{\theta_1}, \tau_{\theta_2}, \tau_{\theta_3}, \tau_d)^T$ where the right subscripts indicate the actuated joint the generalized torque refers to. The virtual work principle [32] makes it possible to write

$$-\boldsymbol{\gamma}^T \delta\boldsymbol{\kappa} + \boldsymbol{\tau}^T \delta\mathbf{q} = 0 \; \forall \delta\mathbf{q} \tag{8}$$

The elimination of $\delta\boldsymbol{\kappa}$ from Equation (8) by means of Equation (5) and the consideration that the resulting expression must hold for any value of $\delta\mathbf{q}$ yield

$$\boldsymbol{\tau} = (\mathbf{J}_k^{-1}\mathbf{J}_q)^T \boldsymbol{\gamma} \tag{9}$$

where

$$(\mathbf{J}_k^{-1}\mathbf{J}_q)^T = \begin{bmatrix} -(a_1 s_{\theta_1} + a_2 s_{(\theta_1+\theta_2)}) & (a_1 c_{\theta_1} + a_2 c_{(\theta_1+\theta_2)}) & 0 & \frac{m_x(a_1 s_{\theta_1} + a_2 s_{(\theta_1+\theta_2)}) - m_y(a_1 c_{\theta_1} + a_2 c_{(\theta_1+\theta_2)})}{a_p(m_y c_\varphi - m_x s_\varphi)} \\ -a_2 s_{(\theta_1+\theta_2)} & a_2 c_{(\theta_1+\theta_2)} & 0 & \frac{a_2(m_x s_{(\theta_1+\theta_2)} - m_y c_{(\theta_1+\theta_2)})}{a_p(m_y c_\varphi - m_x s_\varphi)} \\ 0 & 0 & 0 & \frac{a_3(m_y c_{\theta_3} - m_x s_{\theta_3})}{a_p(m_y c_\varphi - m_x s_\varphi)} \\ 0 & 0 & 1 & 0 \end{bmatrix} \tag{10}$$

The analysis of Equation (9) and of Figures 1 and 2 reveals that, over the platform,

(a) $F_{e,x}$ and $F_{e,y}$ load only the RRC limb, their effects are coupled and do not depend on φ (i.e., on the platform orientation);

(b) $F_{e,z}$ loads the CRS limb through the S-pair and its static effect on links 3 and 4 (see Figure 2) depends on the limb configuration. Moreover, the static equilibrium of the platform reveals that, when $F_{e,z}$ is applied at O_p and the S-pair equilibrates it by applying a force $-F_{e,z}$ at A_2, a torque, M_p, with magnitude $|F_{e,z}\, a_p|$ (see Figure 1) and direction perpendicular to the platform plane (i.e., the plane located by the points O_p, A_p and A_2) arises. M_p must be equilibrated by the reaction in the passive C-pair of the RRC limb. As a consequence, $F_{e,z}$ makes the RRC limb loaded, too, by the torque M_p, whose static effects on links 1 and 2 depend on the platform pose and the limb configuration;

(c) $M_{e,z}$ loads both the limbs and all the links.

[2] Hereafter, the phrase "active force" indicates a force that does work when the mechanism changes its configuration.

During motion, all the components of $\boldsymbol{\gamma}$ ($= -(F_{e,x}, F_{e,y}, F_{e,z}, M_{e,z})^T$) are generated from the inertia forces arising in the mechanism. Therefore, the static analysis must consider all the above-mentioned cases. Regarding case (a), links' internal loads, caused by a unit force $(F_{e,x}, F_{e,y}) = (c_\psi, s_\psi)$ N for $\psi \in [0°, 360°]$, corresponding to $\mathbf{u}_1 = (c_\psi, s_\psi, 0, 0)^T$ N for $\psi \in [0°, 360°]$, applied to the RRC limb at A_1 (see Figures 1 and 2), must be determined for a discretized set of A_1 positions inside the useful workspace. Regarding case (b), links' internal loads, caused by a unit force $F_{e,z}$ (= 1 N), corresponding to $\mathbf{u}_2 = (0, 0, 1, 0)^T$ N, applied at O_p (see Figures 1 and 2), must be determined for a discretized set of O_p positions inside the useful workspace. Regarding case (c), links' internal loads, caused by an unit moment $M_{e,z}$ (=1 Nm), corresponding to $\mathbf{u}_3 = (0, 0, 0, 1)^T$ Nm, applied to the platform at O_p (see Figures 1 and 2), must be determined for a discretized set of O_p positions inside the useful workspace.

3.2. Implementation of Steps (iii) and (iv)

3.2.1. Case (a): Links' Internal Loads Due to $\mathbf{u}_1$

In this case, only links 1 and 2 (Figure 2) are loaded and the static problem is planar. Indeed (Figures 2 and 3), it consists in computing the maximum internal loads, for each admissible RRC limb configuration (i.e., for each position of A_1 in the useful workspace), in a RRC limb locked at the analyzed configuration with the planar force $\mathbf{f}_e = (F_{e,x}, F_{e,y})^T = (c_\psi, s_\psi)^T$ N for $\psi \in [0°, 360°]$ applied at A_1.

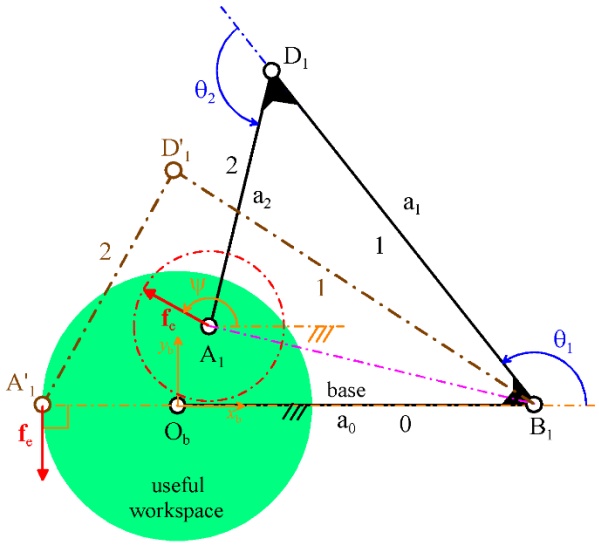

Figure 3. Static problem to solve in case (a).

This problem is quite simple. Indeed, due to the planarity of the problem the non-null internal loads of the two links are only three: the bending moment (M_y), the shear force (S_z), and the axial force (A_x)[3]. Regarding link 2, whatever be the limb configuration, the maximum M_y and S_z always occur at D_1 when $\mathbf{f}_e$ is perpendicular to the link axis (i.e., when $\psi = \theta_1 + \theta_2 \pm 90°$) and their values are $M_{y,2,max} = \pm |\mathbf{f}_e| a_2 = \pm 0.6$ Nm and $S_{z,2,max} = \pm |\mathbf{f}_e| = \pm 1$ N, respectively. Further, the maximum A_x occurs when $\mathbf{f}_e$ is aligned with the link axis (i.e., when $\psi = \theta_1 + \theta_2$ or $\psi = \theta_1 + \theta_2 + 180°$) and its value is $A_{x,2,max} = \pm |\mathbf{f}_e| = \pm 1$ N.

Regarding link 1, at any limb configuration, the maximum M_y occurs either at B_1 when the distance between $\mathbf{f}_e$' s line of action and B_1 is maximum (i.e., when $\mathbf{f}_e$ is perpendicular to the segment A_1B_1 (see Figure 3)), where its value is $M_{y,1} = \pm |\mathbf{f}_e| |(A_1 - B_1)|$, or, for $|(A_1 - B_1)| < a_2$, at D_1 where $M_{y,1} = M_{y,2,max} = \pm |\mathbf{f}_e| a_2$ when $\psi = \theta_1 + \theta_2 \pm 90°$. Anyway,

[3] Hereafter, the internal loads of a beam refer to a local Cartesian system chosen according to the convention 1 that is reported in [28]. This local system has the x axis along the beam axis, the z axis contained in the motion plane (i.e., the $x_b y_b$ coordinate-plane shown in Figure 2), and the y axis perpendicular to the motion plane and pointing toward the reader (i.e., with the same direction of the z_b-coordinate axis shown in Figure 1).

the limb configuration with the maximum $M_{y,1}$ is the one where the point A_1 coincides with the point A'_1 shown in Figure 3. In this configuration, the maximum M_y occurs at B_1 for $\psi = \pm 90°$ and its value is $M_{y,1,max} = \pm |\mathbf{f_e}| |(A'_1 - B_1)| = \pm 1.1$ Nm. Moreover, whatever be the limb configuration, the maximum S_z (A_x) occurs when $\mathbf{f_e}$ is perpendicular (parallel) to the link axis, that is, when $\psi = \theta_1 \pm 90°$ (when $\psi = \theta_1$ or $\psi = \theta_1 + 180°$), and its value is $S_{z,1,max} = \pm |\mathbf{f_e}| = \pm 1$ N ($A_{x,2,max} = \pm |\mathbf{f_e}| = \pm 1$ N). Table 1 summarizes the results of case (a).

Table 1. Maximum non-null influence coefficients due to the unit force $\mathbf{f_e}$ (Figure 3) of case (a).

i (*Link Index*)	$\mathbf{M_{y,i,max}}$ **[Nm]**	$\mathbf{S_{z,i,max}}$ **[N]**	$\mathbf{A_{x,i,max}}$ **[N]**
1	± 1.1	± 1	± 1
2	± 0.6	± 1	± 1

3.2.2. Case (b): Links' Internal Loads Due to $\mathbf{u}_2$

In this case (a unit force $F_{e,z}$ (= 1 N) applied at O_p (see Figures 1 and 2)), the equilibrium of the platform shows that the CRS limb is loaded by the same $F_{e,z}$ (=1 N) applied at the S-pair center. Moreover, it shows that the RRC limb is loaded by a torque, $\mathbf{M_b}$, lying on the motion plane (i.e., the $x_b y_b$ coordinate-plane) and applied at A_1 (see Figure 2). In particular, $\mathbf{M_b}$ has magnitude $|\mathbf{M_b}| = |F_{e,z}\, a_p| = 0.4$ Nm and direction $(\varphi + 90°)$ in the motion plane, that is, $\mathbf{M_b} = |F_{e,z}\, a_p|\, (c_{(\varphi+90°)}, s_{(\varphi+90°)})^T = 0.4(s_\varphi, -c_\varphi)^T$ Nm for $\varphi \in [0°, 360°]$.

Internal Loads in the CRS Limb

In the horizontal part of link 4 (i.e., the segment A_2D_2 (see Figures 1 and 2)), the unit force $F_{e,z}$ (= 1 N) applied at the S-pair center generates a constant shear force $S_{y,4} = F_{e,z} = 1$ N, and a bending moment, $M_{z,4}$, that linearly grows from 0, at A_2, to $M_{z,4,max} = F_{e,z}a_4 = 0.4$ Nm, at D_2. Of course, in the small vertical part of link 4, only a constant axial force equal to $A_{x,4} = -F_{e,z} = -1$ N is present. These values do not depend on the limb configuration.

The node equilibrium at D_2 shows that link 3, at D_2, is loaded by a shear force $S_{y,3} = S_{y,4} = 1$ N, a torsional moment, $M_{x,3}$, whose analytic expression is

$$M_{x,3} = M_{z,4,max} \cos(\theta_4 - 90°) = F_{e,z}a_4 \sin\theta_4 = 0.4 \sin\theta_4 \text{ Nm},$$

and a bending moment, $M_{z,3}$, whose analytic expression is

$$M_{z,3} = M_{z,4,max} \cos\theta_4 = F_{e,z}a_4 \cos\theta_4 = 0.4 \cos\theta_4 \text{ Nm}.$$

As a consequence, in link 3, the shear force $S_{y,3} = 1$ N is constant, and the torsional moment $M_{x,3}$ ($=F_{e,z}a_4 \sin\theta_4 = 0.4 \sin\theta_4$ Nm) is constant, too, but depends on the limb configurations and its maximum $M_{x,3,max} = \pm F_{e,z}a_4 = \pm 0.4$ Nm occurs when $\theta_4 = \pm 90°$. In addition, the bending moment $M_{z,3}$ linearly varies from $F_{e,z}a_4\cos\theta_4$, at D_2, to $(F_{e,z}a_4\cos\theta_4 + S_{y,3}a_3)$, at B_2, and its maximum values occurs at B_2 when θ_4 reaches its maximum value (see Figure 4). In the studied case (Figures 2 and 4), Carnot's theorem applied to the triangle $B_2A_2D_2$ makes it possible to write

$$\cos(\theta_4 - 180°) = \frac{a_3^2 + a_4^2 - \overline{A_2B_2}^2}{2a_3a_4} \text{ with } \left(\overline{A_2B_2}\right)_{min} = a_p - r_{uw} \text{ and } \left(\overline{A_2B_2}\right)_{max} = a_p + r_{uw} \quad (11)$$

which gives $\theta_{4,min} = 194.36°$ and $\theta_{4,max} = 302.09°$. As a consequence, the maximum bending moment is $M_{z,3,max} = F_{e,z}a_4\cos\theta_{4,max} + S_{y,3}a_3 = 0.6125$ Nm.

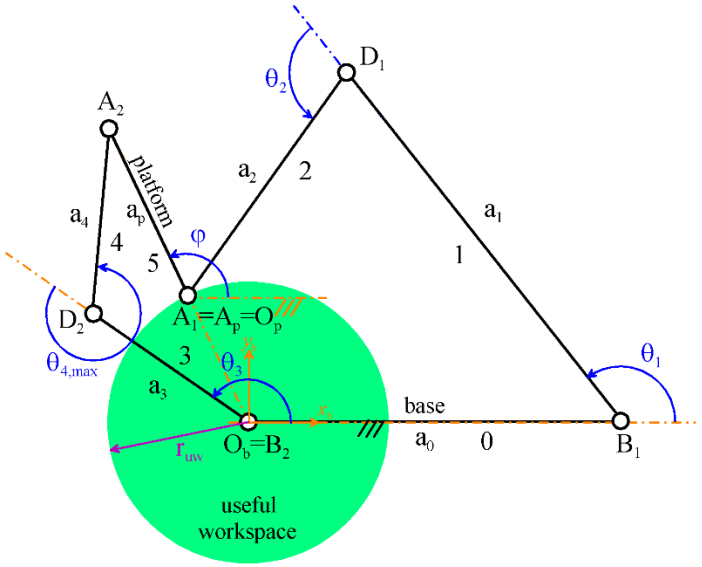

Figure 4. Scaled top view of a LaMaViP's CRS-RRC, sized according to the results of the dimensional synthesis [19], at the configuration where θ_4 reaches its maximum value.

Internal Loads in the RRC Limb

In link 2, the torque $\mathbf{M}_b = |F_{e,z}\, a_p|\, (s_\varphi, -c_\varphi)^T$, for $\varphi \in [0°,360°]$, applied at A_1, generates a constant torsional moment $M_{x,2}$ and a constant bending moment $M_{z,2}$ whose analytic expressions are ($\mathbf{k}_b$ is the unit vector of the z_b-coordinate axis (Figure 1))

$$M_{x,2} = \mathbf{M}_b \cdot \frac{(A_1 - D_1)}{a_2} = |F_{e,z}a_p|(s_\varphi c_{(\theta_1+\theta_2)} - c_\varphi s_{(\theta_1+\theta_2)}) = -|F_{e,z}a_p|c_{(\theta_1+\theta_2-\varphi)} = -0.4c_{(\theta_1+\theta_2-\varphi)}\ \text{Nm}, \quad (12a)$$

$$M_{z,2} = \mathbf{M}_b \cdot \left[\tfrac{(A_1-D_1)}{a_2} \times \mathbf{k}_b\right] = |F_{e,z}a_p|(s_\varphi c_{(\theta_1+\theta_2-90°)} - c_\varphi s_{(\theta_1+\theta_2-90°)}) = |F_{e,z}a_p|s_{(\theta_1+\theta_2-\varphi)} = 0.4s_{(\theta_1+\theta_2-\varphi)}\ \text{Nm} \quad (12b)$$

and depend on the mechanism configuration. Accordingly, the maximum/minimum values of $M_{x,2}$ ($M_{z,2}$) are $M_{x,2,max} = \pm|F_{e,z}\ a_p| = \pm 0.4$ Nm ($M_{z,2,max} = \pm|F_{e,z}\ a_p| = \pm 0.4$ Nm), occur at $\varphi = \theta_1 + \theta_2$ and at $\varphi = \theta_1 + \theta_2 + 180°$ (at $\varphi = \theta_1 + \theta_2 \pm 90°$) and do not depend on the mechanism configuration.

In link 1, the same torque $\mathbf{M}_b = |F_{e,z}\ a_p|\ (s_\varphi, -c_\varphi)^T$, for $\varphi \in [0°,360°]$, transmitted through link 2, is applied at D_1 and generates a constant torsional moment $M_{x,1}$ and a constant bending moment $M_{z,1}$ whose analytic expressions are

$$M_{x,1} = \mathbf{M}_b \cdot \frac{(D_1 - B_1)}{a_1} = |F_{e,z}a_p|(s_\varphi c_{\theta_1} - c_\varphi s_{\theta_1}) = -|F_{e,z}a_p|c_{(\theta_1-\varphi)} = -0.4c_{(\theta_1-\varphi)}\ \text{Nm}, \quad (13a)$$

$$M_{z,1} = \mathbf{M}_b \cdot \left[\frac{(D_1 - B_1)}{a_1} \times \mathbf{k}_b\right] = |F_{e,z}a_p|(s_\varphi c_{(\theta_1-90°)} - c_\varphi s_{(\theta_1-90°)}) = |F_{e,z}a_p|s_{(\theta_1-\varphi)} = 0.4s_{(\theta_1-\varphi)}\ \text{Nm}, \quad (13b)$$

and depend on the mechanism configuration. Accordingly, the maximum/minimum values of $M_{x,1}$ ($M_{z,1}$) are $M_{x,1,max} = \pm|F_{e,z}\ a_p| = \pm 0.4$ Nm ($M_{z,1,max} = \pm|F_{e,z}\ a_p| = \pm 0.4$ Nm), occur at $\varphi = \theta_1$ and at $\varphi = \theta_1 + 180°$ (at $\varphi = \theta_1 \pm 90°$) and do not depend on the mechanism configuration.

Table 2 summarizes the results of case (b).

Table 2. Maximum non-null influence coefficients due to the unit force $F_{e,z}$ (= 1 N) of case (b).

i (*Link Index*)	$M_{x,i,max}$ [Nm]	$M_{y,i,max}$ [Nm]	$M_{z,i,max}$ [Nm]	$S_{y,i,max}$ [N]	$S_{z,i,max}$ [N]	$A_{x,i,max}$ [N]
1	±0.4	-	±0.4	-	-	-
2	±0.4	-	±0.4	-	-	-
3	±0.4	-	0.6125	1	-	-
4	-	-	0.4	1	-	−1

3.2.3. Case (c): Links' Internal Loads Due to $\mathbf{u}_3$

In this case (a unit moment $M_{e,z}$ (=1 Nm) applied at O_p (see Figures 1 and 2)), the equilibrium of the platform shows that the CRS limb is loaded by the force

$$\mathbf{f}_m = -\frac{M_{e,z}}{a_p s_\mu}\begin{pmatrix} c_{(\theta_3+\theta_4)} \\ s_{(\theta_3+\theta_4)} \end{pmatrix} = -\frac{M_{e,z}}{a_p a_4 s_\mu}\begin{pmatrix} m_x \\ m_y \end{pmatrix} \text{ with } \mu = \varphi - \theta_3 - \theta_4, \tag{14}$$

which is applied at the S-pair center and is aligned with link 4 (see Figure 5a), and that the RRC limb is loaded by the force $-\mathbf{f}_m$ applied at A_1 through the C-pair (see Figure 5a).

The maximum and minimum magnitudes of $\mathbf{f}_m$ occur when the angle μ reaches its minimum, μ_{min} (see Figure 5b), and maximum, μ_{max} (see Figure 5c), values, respectively. With reference to Figure 5b,c, in the studied case, the following relationships hold

$$\mu_{min} = 2\arcsin\left(\frac{a_3 - r_{uw}}{2a_4}\right) = 14.3615^\circ,\ \mu_{max} = 2\arcsin\left(\frac{a_3 + r_{uw}}{2a_4}\right) = 122.09^\circ \tag{15}$$

which give

$$|\mathbf{f}_m|_{max} = \frac{M_{e,z}}{a_p s_{\mu_{min}}} = 10.079 \text{ N},\ |\mathbf{f}_m|_{min} = \frac{M_{e,z}}{a_p s_{\mu_{max}}} = 2.95084 \text{ N}. \tag{16}$$

Internal Loads in the CRS Limb

In link 4, the effect of the small vertical part (i.e., the one parallel to the z_b-coordinate axis (Figure 1)) is minor, depends on its length, which has not been defined during the dimensional synthesis, and will be neglected in this static analysis. This assumption brings to consider the force $\mathbf{f}_m$ directly applied at A_2 (see Figure 5a) along the horizontal part of link 4. As a consequence, this load generates only an axial force $A_{x,4} = -|\mathbf{f}_m|$ whose maximum (negative) value is $A_{x,4,max} = -10.079$ N (see Equation (15)).

The node equilibrium at D_2 shows that link 3, at D_2, is loaded by the axial force, $A_{x,3}$, and the shear force, $S_{z,3}$, given by the relationships

$$A_{x,3} = \mathbf{f}_m \cdot \frac{(D_2 - B_2)}{a_3} = -\frac{M_{e,z}}{a_p s_\mu}\left(c_{(\theta_3+\theta_4)}c_{\theta_3} + s_{(\theta_3+\theta_4)}s_{\theta_3}\right) = -\frac{M_{e,z}}{a_p s_\mu}c_{\theta_4} = -2.5\frac{c_{\theta_4}}{s_\mu} \text{ N} \tag{17a}$$

$$S_{z,3} = \mathbf{f}_m \cdot \left[\frac{(D_2 - B_2)}{a_3} \times \mathbf{k}_b\right] = -\frac{M_{e,z}}{a_p s_\mu}\left(c_{(\theta_3+\theta_4)}c_{(\theta_3-90^\circ)} + s_{(\theta_3+\theta_4)}s_{(\theta_3-90^\circ)}\right) = -\frac{M_{e,z}}{a_p s_\mu}c_{(\theta_4+90^\circ)} = 2.5\frac{s_{\theta_4}}{s_\mu} \text{ N} \tag{17b}$$

These loads, at D_2, generate constant axial, $A_{x,3}$, and shear, $S_{z,3}$, forces along link 3 that only depend on the mechanism configuration, and a bending moment $M_{y,3}$ that linearly varies from 0, at D_2, to $-S_{z,3}a_3$, at B_2. Since the angles μ (see Equation (14)) and θ_4 that appear in Equations (17a) and (17b) are not independent (see system (4) and Equation (7)), the determination of the maximum/minimum values of $A_{x,3}$, $S_{z,3}$, and $M_{y,3}$ must be numerically evaluated for a sufficiently high number of mechanism configurations uniformly distributed in the useful workspace and, then, compared. A mash of 3220 positions of A_1(=(x_p, y_p)) uniformly distributed inside the useful-workspace circle have been chosen and, at each A_1 position, Equations (17a) and (17b) have been evaluated for 360 values of the angle φ spaced of 1°. The comparison of the so-computed values yields the diagrams of Figure 6 (The MatLab program that generates Figure 6 can be seen in

Supplementary Materials). The analysis of these diagrams and the ranges spanned by the angles θ_4 and μ (see Equations (11) and (15)) bring to the conclusion that, in link 3, the maximum values of the internal loads can be evaluated as follows

$$A_{x,3,max} = \pm 2.5 \frac{c_{\theta_{4,max}}}{s_{\mu_{min}}} = \pm 5.3545 \text{ N}, \; S_{z,3,max} = 2.5 \frac{s_{270^\circ}}{s_{\mu_{min}}} = -10.079 \text{ N},$$
$$M_{y,3,max} = -S_{z,3,max} a_3 = 4.0316 \text{ Nm}$$

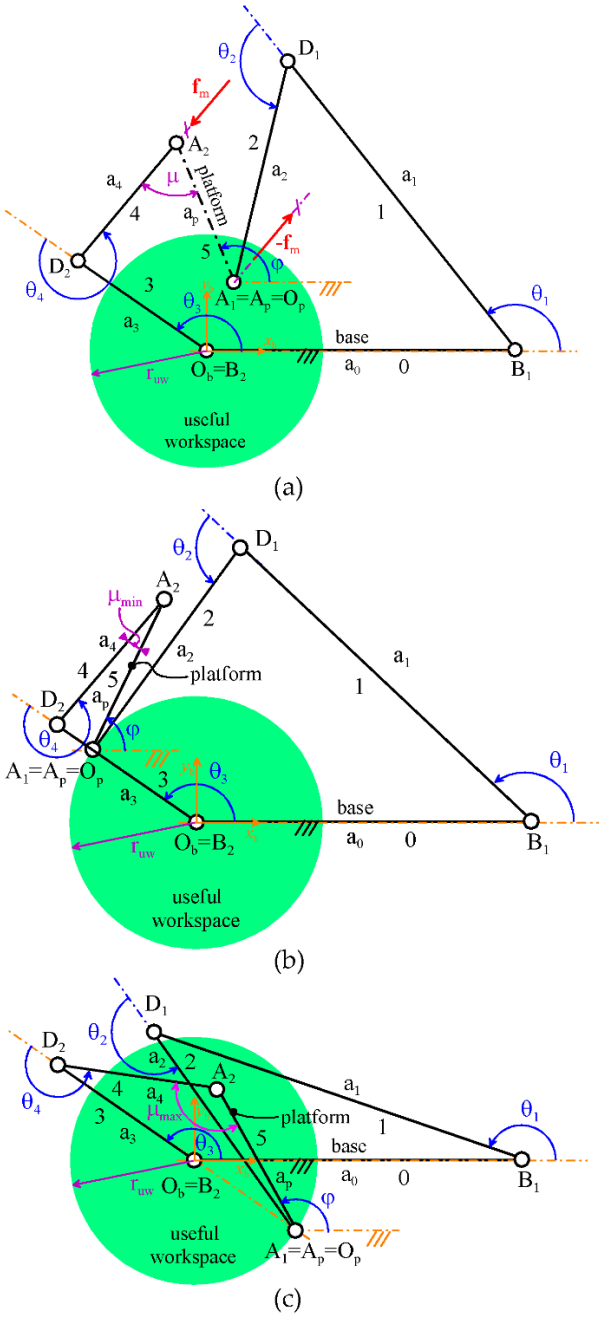

Figure 5. Top view of the studied LaMaViP's CRS-RRC: (**a**) external loads applied to the limbs in the case $M_{e,z}$ = 1 Nm, (**b**) a mechanism configuration with the minimum value of μ, (**c**) a mechanism configuration with the maximum value of μ.

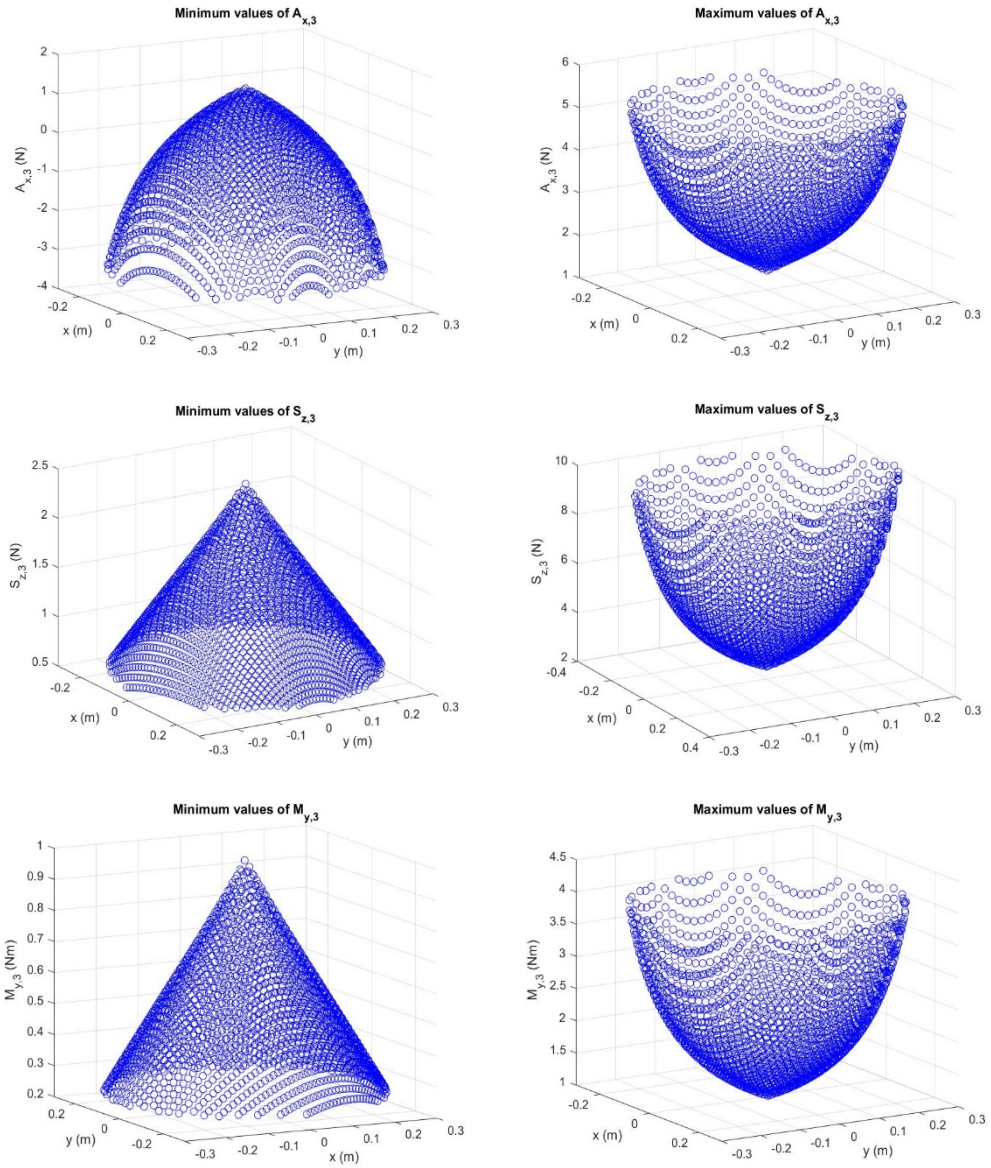

Figure 6. Case $M_{e,z}$ = 1: minimum and maximum values of $A_{x,3}$, $S_{z,3}$, and $M_{y,3}$ computed for 3220 positions of $A_1(=(x_p, y_p))$ uniformly distributed inside the useful-workspace circle.

Internal Loads in the RRC Limb

The comparison of Figures 3 and 5a together with Equation (14) reveals that this is a special case of the above-discussed case (a). Consequently, the maximum values of the internal loads of links 1 and 2 are the product of the influence coefficients of Table 1 by $|\mathbf{f}_m|_{max}$ (see Equation (16)).

Table 3 summarizes the results of case (c).

Table 3. Maximum non-null influence coefficients due to the unit moment $M_{e,z}$ (= 1 Nm) of case (c).

i (*Link Index*)	$\mathbf{M_{x,i,max}}$ **[Nm]**	$\mathbf{M_{y,i,max}}$ **[Nm]**	$\mathbf{M_{z,i,max}}$ **[Nm]**	$\mathbf{S_{y,i,max}}$ **[N]**	$\mathbf{S_{z,i,max}}$ **[N]**	$\mathbf{A_{x,i,max}}$ **[N]**
1	-	±11.087	-	-	±10.079	±10.079
2	-	±6.0474	-	-	±10.079	±10.079
3	-	4.0316	-	-	−10.079	±5.3545
4	-	-	-	-	-	−10.079

3.3. Implementation of Step (v)

The influence coefficients reported in Tables 1–3 must be combined by means of Equation (3) to determine the reference internal loads to use for sizing the links. In order to do this, the values of the coefficients λ_p appearing in Equation (3) must be deduced from the task requirements the machine has to satisfy. Assuming that the design requirements are

- mass of the payload: $m_p = 1$ kg,
- gyration radius of the payload: $\rho = 0.2$ m,
- maximum linear accelerations: $\ddot{a} = 100\ \mathrm{m/s^2}$,
- maximum angular acceleration: $\ddot{\varphi} = 1000\ \mathrm{rad/s^2}$,
- global safety coefficient[4]: $\gamma = 2.5$,

the reference values of the external loads become $F_{e,x} = F_{e,y} = F_{e,z} = \gamma m_p \ddot{a} = 250$ N and $M_{e,z} = \gamma m_p \rho^2 \ddot{\varphi} = 100$ Nm. Accordingly, the influence coefficients of Tables 1 and 2 must be all multiplied by $\lambda_p = 250$ and those of Table 3 by $\lambda_p = 100$; then, the resulting values must be summed. Table 4 reports the reference internal loads resulting from this computation.

Table 4. Reference internal loads to use for sizing the links.

i (*Link Index*)	$M_{x,i,max}$ [Nm]	$M_{y,i,max}$ [Nm]	$M_{z,i,max}$ [Nm]	$S_{y,i,max}$ [N]	$S_{z,i,max}$ [N]	$A_{x,i,max}$ [N]
1	±100	±1383.7	±100	-	±1257.9	±1257.9
2	±100	±754.74	±100	-	±1257.9	±1257.9
3	±100	403.16	153.125	250	−1007.9	±535.45
4	-	-	100	250	-	−1257.9

4. Discussion

The implementation reported in the previous section shows that the proposed method is simple and direct to apply and only in a few cases it really requires numerical evaluations. In particular, it only needs the results of the dimensional synthesis and, differently from the techniques based on global performance indices, it is able to relate directly the task requirements to the links' internal loads.

The analysis of Table 2 reveals that the existence of decoupled motions does not imply a static decoupling between the active forces that cause those motions. Indeed, the unit force $F_{e,z}$ (see Table 2) has a static effect on links 1 and 2 that belong to a limb, the RRC, that has no effect on the platform translation along the z_b-coordinate axis direction. This happens without considering non-ideal phenomena (e.g., the friction in the joints). Furthermore, the found effects are difficult to compensate since the generated torsional, $M_{x,(1,2)}$, and bending, $M_{z,(1,2)}$, moments lie on the RRC-limb motion plane and tend to cause elastic displacements (which, in practice, are vibrations, since all the real external loads are dynamic loads that vary their magnitudes during motion) perpendicular to that plane.

Recognizing static couplings at an early stage of the design procedure with a clear identification of the causes is a peculiarity of the proposed method and is a desirable feature that can orientate the successive design choices. Other design techniques based on the extensive use of multi-body simulation software, together with a trial-and-error sizing procedure, would have found the limb vibration without giving an immediate explanation.

These results prove that the proposed algorithm integrates the design methodologies based on performance indices and/or on extended multibody simulations by solving their lacks.

[4] The global safety coefficient roughly takes into account the loads different from the payload that have not been considered. The designer according to his experience assigns its value.

5. Conclusions

A general technique based on influence coefficients and static analyses has been presented which allows the determination of the input data of the machine-element design (i.e., reference external loads and machine configurations that give the maximum internal load of each component) for non-overconstrained manipulators.

Differently from other techniques, the presented one uses only the results of the dimensional synthesis and does not need any tentative choice, about the materials, the links are made of, and links' cross-sections, to be adjusted during the design procedure.

The proposed technique directly relates task requirements to links' internal loads and is able to reveals dynamic phenomena (e.g., vibrations) that have a negative impact on the machine behavior.

The effectiveness of the proposed technique has been proved by implementing it on a 3T1R parallel manipulator.

Supplementary Materials: The MatLab program that generates Figure 6 is available at https://www.mdpi.com/2075-1702/9/2/27/s1.

Author Contributions: Conceptualization, R.D.G.; methodology, R.D.G.; software, E.Y.; validation, R.D.G. and E.Y.; formal analysis, R.D.G. and E.Y.; project administration, R.D.G.; funding acquisition, R.D.G. All authors have read and agreed to the published version of the manuscript.

Funding: This research was developed at the Laboratory of Mechatronics and Virtual Prototyping (LaMaViP) of Ferrara Technopole and funded by the University of Ferrara (UNIFE), grant number FAR2019.

Institutional Review Board Statement: Not applicable.

Informed Consent Statement: Not applicable.

Data Availability Statement: Not applicable.

Conflicts of Interest: The authors declare no conflict of interest. The funders had no role in the design of the study; in the collection, analyses, or interpretation of data; in the writing of the manuscript, or in the decision to publish the results.

References

1. Hartenburg, R.S.; Denavit, J. *Kinematic Synthesis of Linkages*; McGraw-Hill: New York, NY, USA, 1964; ISBN 9780070269101.
2. Tsai, L.W. *Mechanism Design: Enumeration of Kinematic Structures According to Function*; CRC Press LLC: Boca Raton, FL, USA, 2001.
3. Kong, X.; Gosselin, C.M. *Type Synthesis of Parallel Mechanisms*; Springer: Berlin/Heidelberg, Germany, 2007; ISBN 978-3-642-09118-6.
4. McCarthy, J.M.; Soh, G.S. *Geometric Design of Linkages*; Springer: Berlin/Heidelberg, Germany, 2011.
5. Bhandari, V.B. *Design of Machine Elements*, 3rd ed.; Tata McGraw-Hill: New Delhi, India, 2010.
6. Jiang, W. *Analysis and Design of Machine Elements*; Wiley: Singapore, 2019.
7. Ashby, M.F. *Materials Selection in Mechanical Design*, 5th ed.; Butterworth-Heinemann: Burlington, MA, USA, 2016.
8. Gosselin, C.; Angeles, J. Singularity analysis of closed-loop kinematic chains. *IEEE Trans. Robot. Autom.* **1990**, *6*, 281–290. [CrossRef]
9. Zlatanov, D.; Fenton, R.G.; Benhabib, B. A Unifying Framework for Classification and Interpretation of Mechanism Singularities. *J. Mech. Des.* **1995**, *117*, 566–572. [CrossRef]
10. Di Gregorio, R. A Review of the Literature on the Lower-Mobility Parallel Manipulators of 3-UPU or 3-URU Type. *Robotics* **2020**, *9*, 5. [CrossRef]
11. Yoshikawa, T. Manipulability of Robotic Mechanisms. *Int. J. of Rob. Res.* **1985**, *4*, 3–9. [CrossRef]
12. Klein, C.A.; Blaho, B.E. Dexterity Measures for the Design and Control of Kinematically Redundant Manipulators. *Int. J. Robot. Res.* **1987**, *6*, 72–83. [CrossRef]
13. Gosselin, C.; Angeles, J. A Global Performance Index for the Kinematic Optimization of Robotic Manipulators. *J. Mech. Des.* **1991**, *113*, 220–226. [CrossRef]
14. Tanev, T.; Stoyanov, B. On the performance indexes for robot manipulators. *Probl. Eng. Cybern. Robot.* **2000**, *49*, 64–71.
15. Merlet, J.P. Jacobian, Manipulability, Condition Number, and Accuracy of Parallel Robots. *J. Mech. Des.* **2006**, *128*, 199–206. [CrossRef]
16. Moreno, H.A.; Saltaren, R.; Carrera, I.; Puglisi, L.J.; Aracil, R. Ìndices de Desempeño de Robots Manipuladores: Una revisión del Estado del Arte. *Rev. Iberoam. Automática Inf. Ind.* **2012**, *9*, 111–122. [CrossRef]

17. Patel, S.H.; Sobh, T. Manipulator Performance Measures—A Comprehensive Literature Survey. *J. Intell. Robot. Syst.* **2014**, *77*, 547–570. [CrossRef]
18. Rosyid, A.; El-Khasawneh, B.; Alazzam, A. Review article: Performance measures of parallel kinematics manipulators. *Mech. Sci.* **2020**, *11*, 49–73. [CrossRef]
19. Di Gregorio, R.; Cattai, M.; Simas, H. Performance-Based Design of the CRS-RRC Schoenflies-Motion Generator. *Robotics* **2018**, *7*, 55. [CrossRef]
20. Simas, H.; Di Gregorio, R. Position analysis, singularity loci and workspace of a novel 2PRPU Schoenflies-motion generator. *Robotics* **2018**, *37*, 141–160. [CrossRef]
21. Asada, H. A Geometrical Representation of Manipulator Dynamics and Its Application to Arm Design. *J. Dyn. Syst. Meas. Control.* **1983**, *105*, 131–142. [CrossRef]
22. Yoshikawa, T. Dynamic manipulability of robot manipulators. *J. Rob. Sys.* **1985**, *2*, 113–124.
23. Wiens, G.J.; Scott, R.A.; Zarrugh, M.Y. The Role of Inertia Sensitivity in the Evaluation of Manipulator Performance. *J. Dyn. Syst. Meas. Control.* **1989**, *111*, 194–199. [CrossRef]
24. Chiaacchio, P.; Concilio, M. The dynamic manipulability ellipsoid for redundant manipulators. In *Proceeding of the 1998 IEEE International Conference on Robotics and Automation (ICRA), Leuven, BE, 20 May 1998*; IEEE: Piscataway, NJ, USA, 1998; pp. 95–100. [CrossRef]
25. Di Gregorio, R.; Parenti-Castelli, V. Dynamic performance indices for 3-dof parallel manipulators. In *Advances in Robot Kine-Matics*; Lenarcic, J., Thomas, F., Eds.; Springer: Dordrecht, The Netherlands, 2002; pp. 11–20.
26. Mo, J.; Shao, Z.; Guan, L.; Xie, F.; Tang, X. Dynamic performance analysis of the X4 high-speed pick-and-place parallel robot. *Robot. Comput. Manuf.* **2017**, *46*, 48–57. [CrossRef]
27. Angeles, J. *Fundamentals of Robotic Mechanical Systems*, 4th ed.; Springer: New York, NY, USA, 2014.
28. Wunderlich, W.; Pilkey, W.D. *Mechanics of Structures: Variational and Computational Methods*, 2nd ed.; CRC Press: Boca Raton, FL, USA, 2002.
29. Uicker, J.J.; Pennock, G.R.; Shigley, J.E.; McCarthy, J.M. *Theory of Machines and Mechanisms*, 5th ed.; Oxford University Press: New York, NY, USA, 2016.
30. Hervé, J.M. The mathematical group structure of the set of displacements. *Mech. Mach. Theory* **1994**, *29*, 73–81. [CrossRef]
31. Di Gregorio, R. A Novel Single-Loop Decoupled Schoenflies-Motion Generator: Concept and Kinematics Analysis. In *Advances in Service and Industrial Robotics*; Ferraresi, C., Quaglia, G., Eds.; Mechanisms and Machine Science Series; Springer: New York, NY, USA, 2018; Volume 49, pp. 11–18. ISBN 978-3-319-61275-1. [CrossRef]
32. Salençon, J. *Virtual Work Approach to Mechanical Modeling*; Wiley: Hoboken, NJ, USA, 2018.